



This is the accepted manuscript made available via CHORUS. The article has been published as:

Threshold displacement energies in graphene and single-walled carbon nanotubes

Andrew Merrill, Cory D. Cress, Jamie E. Rossi, Nathanael D. Cox, and Brian J. Landi

Phys. Rev. B **92**, 075404 — Published 3 August 2015

DOI: [10.1103/PhysRevB.92.075404](https://doi.org/10.1103/PhysRevB.92.075404)

Threshold displacement energies in graphene and single-walled carbon nanotubes

Andrew Merrill,¹ Cory D. Cress,² Jamie E. Rossi,¹ Nathanael D. Cox,^{1,3} and Brian J. Landi^{1,4}

¹*NanoPower Research Laboratory, Rochester Institute of Technology, Rochester, NY 14623*

²*Electronics Science and Technology Division, United States Naval Research Laboratory, Washington, DC 20375*

³*Department of Microsystems Engineering, Rochester Institute of Technology, Rochester, NY 14623*

⁴*Department of Chemical Engineering, Rochester Institute of Technology, Rochester, NY 14623*

The threshold displacement energy E_d has been determined for graphene and 216 different (n, m) single-walled carbon nanotube chiralities, with $5 \leq n \leq 20$ and $0 \leq m \leq n$, under several model conditions using classical molecular dynamics. The model conditions vary by particle (electron or carbon ion), empirical potential (two parameterizations of Tersoff and one Brenner), and momentum transfer direction (towards or away from the nanotube axis). For electron irradiation simulations, E_d exhibits a smoothly varying chirality dependence and a characteristic curvature influenced by the momentum transfer direction. Changing the empirical potential shifts the magnitude of E_d , but the trend is preserved for electron simulations. However, the perturbation in the knock-on dynamics introduced by the carbon ion leads to E_d trends that diverge from the equivalent electron simulation. Thus, the ion interaction has a non-negligible effect on the dynamics of the collision and leads to E_d values that can distinctly vary depending on the selected carbon nanostructure.

PACS numbers: 61.80.Az, 61.80.Jh, 61.46.Fg, 61.48.Gh

I. INTRODUCTION

Graphene and carbon nanotubes are promising candidate materials for use in a diverse range of electronic applications on account of their unique physical properties.^{1,2} Tailoring these properties for specific applications using electron or ion irradiation is a proposed method for realizing their full potential,³ and has prompted intense research on both experimental and theoretical fronts to understand their radiation response. In addition, understanding the effects of electron and ion irradiation on carbon nanostructures has practical implications for devices and structures exposed to radiation environments.^{4–6}

The minimum kinetic energy an atom must acquire to be displaced from its lattice site is the threshold displacement energy E_d . It plays a central role within the theoretical frameworks^{7,8} and computational tools⁹ used to calculate and predict the effects of different types of irradiation on the physical properties of a material. Precise knowledge of E_d as a function of chirality is a critical experimental input parameter to enable irradiation-induced modification of carbon nanostructure properties, such as controlled vacancy formation or direct substitutional doping.¹⁰ Larger threshold energies imply higher radiation stability and a chiral map of E_d could bring important new insights to help guide the design and modification of these nanostructured materials for use in radiation environments.

II. BACKGROUND

The E_d of graphene and single-walled carbon nanotubes (SWCNTs) has been studied computationally by several groups using both electron^{11–16} and ion^{17–20} irradiation, classical^{19,20} and quantum-based^{11–18} molecular dynamics (MD) methods, and different directions of mo-

mentum transfer^{11,14,15,21} to the primary knock-on atom (PKA). Several of these results are tabulated in Table I and indicate most studies have focused on electron irradiation simulations using density-functional theory (DFT) MD or DFT-based MD methods. In all cases, the range of chiralities investigated for SWCNTs has been limited to a subset of achiral (armchair and zigzag) nanotubes, with the most extensive chirality dependent study previously reported by Krasheninnikov *et al.*¹³ where E_d was determined for 10 armchair ($3 \leq n \leq 12$) and 16 zigzag ($5 \leq n \leq 20$) chiralities.

In this work, we perform a systematic study on the chirality dependence of E_d for SWCNTs using classical molecular dynamics. While we recognize the limitations in using classical MD to quantify E_d , trading high accuracy for computational speed using classical MD enabled exploration of chirality dependent irradiation effects in carbon nanostructures over a significantly larger set of chiralities compared to any previously reported studies. Therefore, the primary focus and highlight of these results will be the comprehensive nature of the sample set and the chirality dependent E_d trends that are revealed.

We compute the changes in E_d with respect to the incident particle (electron vs. carbon ion), empirical potential (two parameterizations of Tersoff²³ and one Brenner²⁴), and momentum transfer direction (radially inward vs. radially outward). For each case, the graphene E_d is also determined, providing a consistent relative comparison for all model conditions investigated.

III. COMPUTATIONAL METHODS

The displacement energy of an atom from its lattice is a function of many factors including angle of incidence, irradiation source, and temperature; the minimum at a given temperature is the threshold displacement energy.

TABLE I. Published threshold displacement energy values for graphene and SWCNTs obtained with different molecular dynamics methods, irradiation sources, and directions of radial momentum transfer.^a

Nanostructure	$\Phi_X^{\hat{r}}$ Model ^b	MD Method	E_d (eV)
Graphene	Φ_C	EP ^c	22.20 ^d
Graphene	Φ_e	DFTB ^e	$\sim 22^f$
Graphene	Φ_e	DFTB	$\sim 23^g$
Graphene	Φ_e	DFT ^h	22.03 ⁱ
Graphene	Φ_e	DFT	19.0, ^j 12.0 ^k
SWCNT	Φ_C	EP	17.59 ^l
SWCNT	Φ_e^+	TB ^m	$\sim 17^n$
SWCNT	Φ_e^+	TB	$\sim 7-12^o$
SWCNT	Φ_e^+	DFTB	$\sim 15-22^p$
SWCNT	Φ_e^+	DFTB	$\sim 17-19^q$

^a Only relevant for SWCNT irradiation

^b Symbolic notation described in text

^c Empirical potential

^d Reference 19

^e Density functional tight binding

^f Reference 13

^g Reference 14

^h Density functional theory

ⁱ Reference 22

^j Reference 16, armchair (AC) edge

^k Reference 16, zigzag (ZZ) edge

^l Reference 20, simulated with a 216 atom, (9, 0) ZZ SWCNT

^m Tight binding

ⁿ Reference 11, simulated with a 24 Å, (5, 5) AC SWCNT

^o Reference 12, simulated with (3, 3) to (12, 12) AC SWCNTs

^p Reference 13, simulated with 12–13 Å, (3, 3) to (12, 12) AC SWCNTs

^q Reference 13, simulated with 12–13 Å, (5, 0) to (20, 0) ZZ SWCNTs

To accurately determine E_d through simulation, it must be determined as an average over many simulated measurements.^{25–27} One approach to achieving this is a fixed-interval energy ramp in which the kinetic energy of the PKA or incident ion is increased in fixed intervals over a range of kinetic energies. The simulation is repeated at each energy with slightly different initial conditions and the results averaged. This approach is capable of pinpointing E_d to a high precision, but becomes impractical for large datasets due to its time consuming nature. A more rapid approach uses a *binary search*-like algorithm to pinpoint *candidate* E_d values, allowing exploration of much larger datasets, but at the expense of precise knowledge of where the E_d lies on the displacement probability curves. For this study, we engaged both methods but emphasize the latter approach and developed a heuristic algorithm for determining E_d (see Supplemental Material²⁸ for details of the fixed-interval energy ramp method and results). Based on our knowledge of the variability in E_d arising due to slight perturbations in the initial conditions,^{25–27} the candidate E_d value is determined using a binary search algorithm, and subsequently used to launch a new binary search at some fixed offset below the original candidate E_d . Only after the same candidate E_d value is found repeatedly do we accept it as *the* E_d value

reported in this study.

We developed a computational toolkit for studying ion and electron irradiation of graphene and SWCNTs and used it to automate the simulations employing LAMMPS²⁹ as the molecular dynamics “engine” and implemented our heuristic approach to determine E_d across a large number of chiralities. To facilitate the discussion of our results, we define a symbolic notation that identifies the irradiation source and implicitly identifies the nanostructure along with the direction of momentum transfer from irradiation source to the PKA in SWCNTs. The symbolic notation is $\Phi_X^{\hat{r}}$, where X denotes the ion chemical symbol for ion irradiation or e for electron irradiation. For SWCNTs, $\hat{r} = +$ or $-$ representing momentum transfer from the irradiation source to a PKA directed radially outward or inward, respectively. Figure 1(a) provides visual representation of the symbolic notation. For graphene irradiation simulations, \hat{r} is not specified on account of its planar symmetry.

The molecular dynamics simulations begin by reading simulation parameters from an input data file. After the nanotube structure data is generated, the structure energy is minimized within LAMMPS. A target PKA is randomly selected from a 20 Å region about the center of the nanotube and then the entire nanotube is rotated to align the PKA along the top (bottom) of the nanotube to effect a normally incident PKA collision with an ion or electron fired vertically downward, displacing the PKA radially in (out). The structure is equilibrated to the desired temperature for 0.5 ps followed by a free molecular dynamics run for 1.0 ps.

To simulate ion irradiation, an ion is positioned outside the interaction range of the empirical potential and assigned an initial velocity such that the ion intercepts the PKA with a well-defined energy and angle of incidence. Due to the large relative mass difference between an electron and a target atom, electron irradiation is modeled by giving the PKA an instantaneous initial velocity to simulate an electron-PKA collision with an energy transfer equal to the PKA kinetic energy and the angle of incidence defined by the velocity direction, similar to the methods described by others.^{11,13,14}

In the present study, only normally incident collisions are considered, which for SWCNTs corresponds to two physical situations: one in which the PKA is directed radially outward away from the nanotube axis, Φ_X^+ , the other directed radially inward towards the nanotube axis, Φ_X^- . Experimentally, with an ion or electron beam directed downward on a sample, the two physical situations correspond to irradiated atoms on the bottom and top of the SWCNT, respectively. For electron irradiation simulations, both outward and inward normally incident models are considered in SWCNTs. Φ_C^+ model results are not included in this study on account of symmetry considerations and the nature of the ion trajectory.

Nine combinations of empirical potential, irradiation particle, and direction of radial momentum transfer to the PKA were studied. For each set of conditions, the

threshold displacement energy of 216 different SWCNT chiralities were computed with $\mathbf{C}_h = (n, m \leq n)$ and n ranging from 5–20. The nanotube length was ~ 120 Å across all chiralities. The final ~ 5 Å of each end was fixed, followed by a ~ 10 Å region that was thermostatted. Temperature was controlled with the Berendsen³⁰ thermostat with time constant $\tau = 5$ fs. The temperature in the thermostatted regions was held at 0 K. Figure 1(a) shows our simulation setup. The nanotube was oriented with its axis aligned along the z -axis. Fixed boundaries were used along the z -axis, while shrink-wrapped³¹ boundaries were used along the x - and y -axis. The ion was fired downward on the nanotube in the negative y direction into the plane of the page.

A. Empirical Potentials Overview

Three empirical potentials for carbon bonding were studied: the original Tersoff²³ potential, a Tersoff potential optimized for lattice dynamics and phonon thermal transport,³² and the second generation reactive empirical bond order (REBO) potential of Brenner *et al.*²⁴ These are identified as the Tersoff, Tersoff-2010, and Brenner potentials, respectively.

The Tersoff and Tersoff-2010 potentials modified with the Ziegler-Biersack-Littmark (ZBL) universal screening function³³ were used for the $\Phi_{\bar{C}}$ simulations and are identified as the Tersoff/ZBL and Tersoff-2010/ZBL potentials, respectively. A ZBL modified Brenner potential was not readily available for use in LAMMPS and therefore all Brenner-based simulations were carried out using its non-ZBL modified form.

B. Heuristic Analysis

The heuristic determination of E_d is guided by user defined constraints and accumulated experience from scrutinizing hundreds of simulation results. The analysis for a given chirality starts by running the MD simulation with the kinetic energy of the ion or electron initialized to an energy below that needed to generate a displacement, which in the current study is ~ 30 eV for ion irradiation and ~ 15 eV for electron irradiation since it is applied directly to the PKA. The kinetic energy transferred to the PKA at knock-on and its final defect state are determined during the post-processing data analysis, including a running history of all incident kinetic energies, which are stored in memory to a precision of 10 meV. Pertinent PKA statistics, such as the maximum kinetic energy attained at knock-on and final displacement at the end of the simulation, are mapped to each incident ion kinetic energy. No incident ion kinetic energy is simulated more than once for a given trial set. The PKA displacement must exceed 4 Å at the end of the simulation to be considered a displacement event.

C. Experimental Considerations

The objective of this work is to provide simulation data generated with conditions that permit direct comparison to the growing body of experimental data of normally incident electron or ion irradiation damage in carbon nanostructures. Therefore, we simulate two normally incident orientations, in which the particle (carbon or electron) is directed downward on a SWCNT leading to a PKA displacement in the radially inward direction towards the SWCNT axis. Our third series of simulation data, in which simulated electron irradiation causes a radially outward displacement, provide additional insight into the mechanisms that dictate the chirality-dependent E_d . Additionally, these simulations expand the large set of simulation studies that exclusively consider this radially outward irradiation configuration. Ultimately, we find good agreement between our simulated results and recently reported experimental data based on high-resolution scanning transmission electron microscopy.³⁴

IV. RESULTS AND DISCUSSION

Figure 1(b) depicts the SWCNT chirality dependence of E_d for each set of conditions as color maps in $\mathbf{C}_h = (n, m)$ chirality space, in which each pixel is mapped to a color corresponding to its calculated E_d . Nine chiral maps are included, one for each combination of empirical potential, irradiation particle, and direction of radial momentum transfer to the PKA, and are scaled to the same colorbar to allow direct comparisons between color and E_d value. Each column in Fig. 1(b) represents a different empirical potential while each row is a different combination of incident particle and momentum transfer direction. The differences in E_d between columns clearly demonstrate an increasing E_d trend, from left to right, and that the accuracy of E_d values determined from classical MD hinges upon the quality of the empirical potential employed. Therefore, we focus our attention on the general trends observed for a given potential and those common among all potentials rather than the absolute E_d values obtained.

For a given column (i.e., potential), the variations in E_d between color maps is less pronounced. However, if we compare the chirality dependence of E_d between color maps in row 1 (Φ_e^+) and row 2 (Φ_e^-) for a given column, subtle trends in E_d emerge, pointing to the dependence on the direction of radial momentum transfer. Specifically, for the PKA directed radially outward (Φ_e^+), the values of E_d are less near and along $n = m$ (armchair) than those along $n, m = 0$ (zigzag). This trend is nearly completely reversed for the PKA directed radially inward (Φ_e^-). In both cases for $n \neq m$ (chiral), E_d transitions smoothly between the armchair and zigzag chiralities. We observe this trend in both parameterizations of the Tersoff potentials and the Brenner potential. The outcome is more convoluted in the case of $\Phi_{\bar{C}}$ due

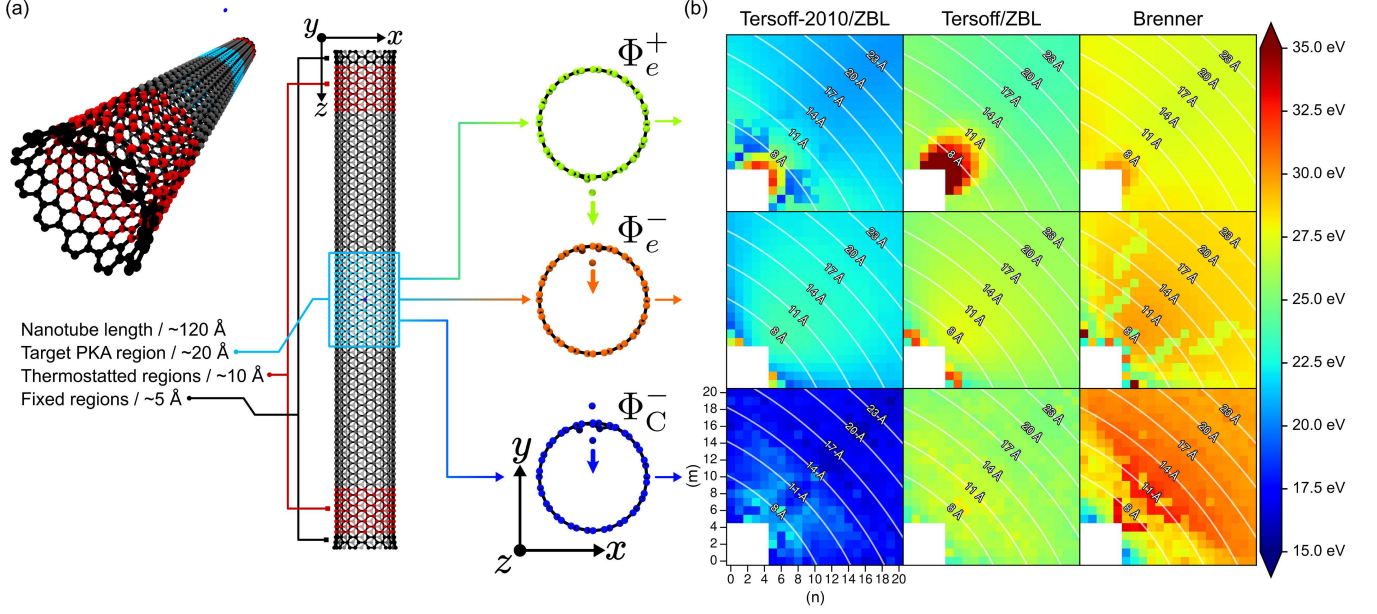


FIG. 1. (Color online) (a) Perspective view and top view schematic of the simulation setup. The black regions of the SWCNT are held fixed during the simulation, the red regions are thermostatted, and the gray and blue regions evolve freely over the course of the simulation. The target PKA is selected randomly from the atoms in the blue region. Arrows branching out from the target PKA region point to snapshots of the three variations in model conditions (axial view) involving different irradiation particles (electron or carbon ion) and direction of momentum transfer (radially in (-) vs. out (+)) along with its corresponding symbolic representation for the model: Φ_e^+ , Φ_e^- , Φ_C^- . (b) Chirality mapped, threshold displacement energies across nine different combinations of irradiation particle, direction, and empirical potential. The rows correspond to the combination of particle and direction as indicated by the axial view snapshot and symbolic notation (defined in the text). Constant diameter contours are shown to highlight the diameter dependence. The right-handed chiralities have been mapped to the left-handed chiralities to effect a full chirality map.

to the presence of the ion, which changes the knock-on dynamics. As the color maps in row 3 (Φ_C^-) of Fig. 1(b) demonstrate, the E_d chirality dependence becomes visually indiscernible at diameters $d_t \gtrsim 12$ Å, above which only a diameter dependence is seen.

Figure 2 maps the E_d for Φ_e^+ , Φ_e^- , and Φ_C^- from Fig. 1(b) collected across all three potentials to diameter dependent trends in Figs. 2(a), 2(b), and 2(c), respectively. It is clear that the optimized Tersoff-2010 parameters reduces the overall displacement threshold as evidenced by the reduction in E_d when comparing each simulation set to the original Tersoff. Furthermore, the Tersoff-2010 potential is more sensitive to the ion as suggested by a reduction in E_d nearly seven times larger than the reduction in the Tersoff potential in comparing the Φ_C^- irradiation results to the electron irradiation results under the same potential. Based on the Φ_C^- simulations with the Tersoff and Tersoff-2010 potentials, the ZBL correction leads to a uniform reduction in E_d of ~ 2 –3 eV across all chiralities and we expect the same to be true of the Brenner-based simulations involving the carbon ion.

Comparing the electron irradiation simulations [Φ_e^+ in Fig. 2(a) vs. Φ_e^- in Fig. 2(b)], we observe that the change in direction of the radial momentum transfer gives rise

to a change in curvature in the diameter dependent E_d trends. The most impactful aspects of these trends are that the achiral E_d values form the lower and upper E_d bounds across nearly all diameters and the achiral *type* forming the upper (lower) bound changes from zigzag (armchair) when the radial momentum transfer direction changes from Φ_e^+ to Φ_e^- .

Comparing the electron and carbon ion irradiation simulations with radially inward PKA momentum transfer [Φ_e^- in Fig. 2(b) vs. Φ_C^- in Fig. 2(c)], we observe a reduction in the graphene E_d for all three interatomic potentials and a reduction in the average SWCNT E_d for both Tersoff parameterizations which include the ZBL correction. The fact that the graphene E_d value reduces slightly for all three potentials suggests that the ion continues to repel the PKA following knock-on (or screens the attractive forces that normally return the PKA to its original lattice site) thereby reducing the peak kinetic energy needed to be displaced. In the Tersoff/ZBL Φ_C^- results, we observe more randomness in E_d for chiral SWCNTs, likely due to slight misalignment in the ion trajectory, but the bounding of the E_d values by the armchair SWCNTs (gray filled) at the upper end and by the zigzag SWCNTs (black filled) at the lower end, is preserved. Therefore, this parameterization suggests essen-

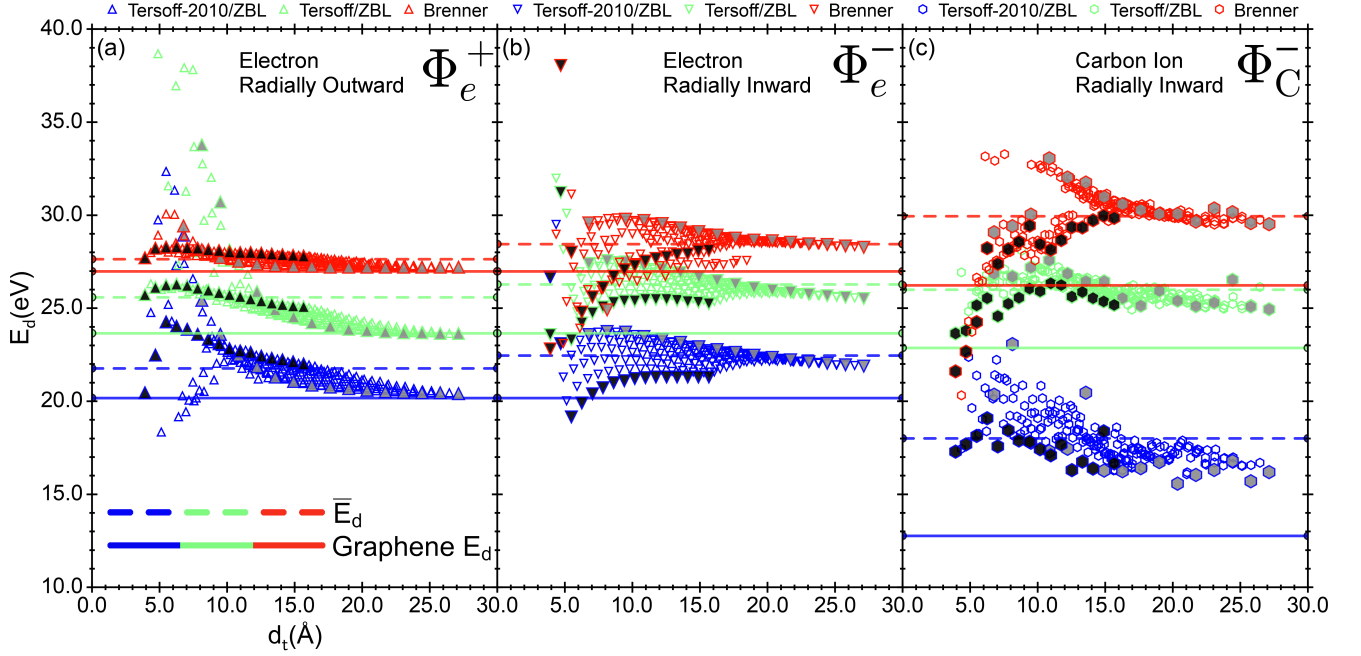


FIG. 2. (Color online) Threshold displacement energy E_d as a function of nanotube diameter for nine combinations of irradiation particles, direction, and empirical potentials. The E_d for electron irradiation with PKA momentum transfer directed radially (a) outward, away from the nanotube axis and (b) inward, towards the nanotube axis. (c) Carbon ion irradiation with ion-PKA momentum transfer directed radially inward. The symbolic notation (Φ_e^+ , Φ_e^- , Φ_C^-) is defined in the text. The zigzag chirality markers are filled in with black and the armchair markers with gray. The dashed lines show the mean E_d (\bar{E}_d) values for each set of conditions. The solid lines are the E_d values obtained for graphene at each simulated irradiation condition.

tially no difference, within error, between the E_d for electron and carbon ion irradiations. In contrast, the Tersoff-2010/ZBL parameterization results in Φ_C^- E_d values that are considerably smaller (2-7 eV) than the corresponding Φ_e^- results and the achiral SWCNTs only set the lower E_d bound. These findings lead to significant uncertainty regarding the dynamics of near-threshold carbon ion irradiations. Depending on the choice of potential, the curvature of the SWCNTs has minimal effect on the E_d for carbon ion irradiations (Tersoff/ZBL) or a very significant effect (Tersoff-2010/ZBL), and therefore warrants additional *ab initio* or experimental investigation.

We calculated and analyzed a number of equilibrium (before knock-on) and time-dependent (following knock-on) structure properties of the PKA to ascertain the physical origin of the chirality and diameter dependent trends as well as their dependence on the direction of radial momentum transfer to the PKA. The results reveal a compelling correlation between the E_d trends and the median PKA nearest-neighbor bond length. Figure 3(a) shows a snapshot 5 fs following simulated knock-on of the time-dependent PKA bond lengths for all 216 chiralities for both Φ_e^- and Φ_e^+ simulations. Following knock-on, the diameter and chirality dependent trends of the median bond length transforms in a manner consistent with the diameter dependent trends of the simulated E_d for both Φ_e^- and Φ_e^+ simulations. Specifically, we see that

the diameter dependent trends of E_d are mirrored across all three bond lengths for both Φ_e^- and Φ_e^+ , with decreasing (increasing) E_d /bonds with increasing d_t for Φ_e^+ (Φ_e^-) simulations. Next, we note that the spread in E_d across each chiral series ($n, m \leq n$) decreases with increasing n and a similar trend is observed for the spread in the chiral series for the median bond length (see Fig. 3(a)). However, the most convincing argument pointing to a physical connection between the PKA E_d and median bond length is the correlation in the upper and lower bounds of both the E_d and median bond length data. In this case, the achiral SWCNTs align with the upper and lower bounds in the electron irradiation simulations. Also, an interchange of the achiral *type* (armchair vs. zigzag) forming the upper and lower bounds is evident upon changing the direction of the radial momentum transfer to the PKA. Thus, the physical origin of the E_d trends appear to be correlated to the time-dependent evolution of the median PKA bond lengths.

A discussion of the bond orientation of the PKA's nearest-neighbor bonds relative to the SWCNT axis may provide insight. Figure 3(b) shows 2D projections onto the PKA tangent plane of three different equilibrium orientations of the PKA and its three nearest-neighbor bonds as the chiral angle θ_c changes from 0° (zigzag) to 15° (chiral) to 30° (armchair). For zigzag SWCNTs, the 2D projection of one PKA bond vector (labeled bond

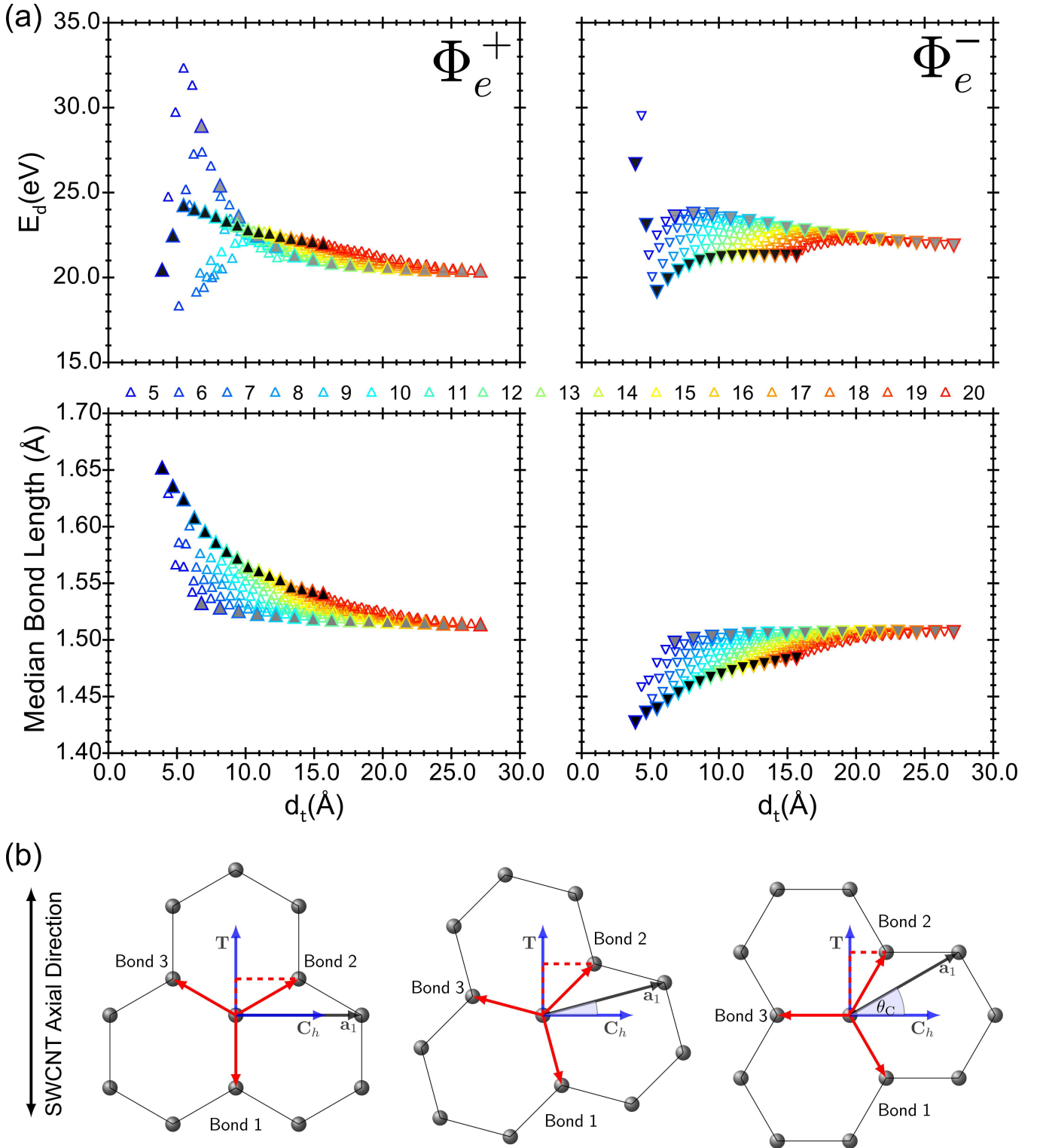


FIG. 3. (Color online) (a) Threshold displacement energy E_d and snapshots of the time-dependent changes in the median PKA nearest-neighbor bond length 5 fs following simulated knock-on for electron irradiation simulations. The zigzag chirality markers are filled in with black and the armchair markers with gray. (b) Schematic diagram showing 2D projections of the PKA and its nearest-neighbors onto the tangent plane of the PKA, highlighting the change in the orientation of the PKA's three nearest-neighbor bond vectors with respect to the SWCNT chiral vector \mathbf{C}_h and translation vector \mathbf{T} , as the chiral angle increases from 0° ($m = 0$) to 30° ($m = n$) for a given chiral series n . The bond vectors of the PKA's three nearest-neighbor atoms are shown in red. The projection of the bond 2 vector onto the translation vector is represented by the dashed red line in each orientation.

1) lies parallel to the SWCNT axis (represented by the translation vector \mathbf{T}) and exhibits the least strain, while the 2D projections of bonds 2 and 3 are oriented with components along the chiral vector \mathbf{C}_h leading to larger bond strain compared to bond 1. As θ_c increases from 0° ($m = 0$) to 30° ($m = n$), for a given chiral series n , Fig. 3(b) shows that the components of the bond vectors for bonds 1 and 3 along \mathbf{C}_h (\mathbf{T}) increase (decrease) with increasing m , indicating a corresponding increase in bond strain with increasing m , while the projection of the bond vector for bond 2 along \mathbf{C}_h (\mathbf{T}) decreases (increases) with increasing m , implying decreasing bond strain with increasing m . Thus, the change in bond 2 strain is opposite that of bonds 1 and 3, suggesting that the physical origin of the correlation of E_d with the median bond length is mediated by the change in the strain in the bond whose projection onto the translation vector increases with increasing chiral angle.

The combined E_d dependence on the direction of radial momentum transfer and chirality/diameter trends adds a new dimension to how reported threshold displacement energies of SWCNTs are interpreted and used for other calculations. Although the diameter and chirality dependence has been previously investigated¹³, the change in the chirality dependence due to the change in the direction of radial momentum transfer has not been previously reported and has been revealed through the present time-dependent structure analysis.

The results from Fig. 2(b) show that the diameter dependent trends in E_d are consistent with the experimental findings of Warner *et al.*³⁴, which demonstrated SWCNTs exhibit increasing irradiation stability with increasing diameter under electron irradiation from a HRTEM. As their HRTEM images show, the pristine SWCNTs were irradiated with electrons directed towards the SWCNT. While many of the images suggest the first defects were generated along the SWCNT edge, any normally incident irradiation scenarios would be more consistent with the Φ_e^- irradiation simulations and not the Φ_e^+ results. As such, our findings reveal consistency with reported experiments investigating irradiation stability of SWCNTs through simulations consistent with the reported experimental setup. None of the reported E_d electron irradiation simulations summarized in Table I have considered the scenario with the PKA momentum transfer directed radially inward. Interestingly, the strong correlation between our computational $\Phi_e^- E_d$ trends and experimental results illustrate the importance of modeling both incident directions.

The E_d values obtained through our heuristic analysis represent the minimum kinetic energy required to create a defect. However, in practice, due to the probabilistic nature of the ion collision with the PKA, there can be a range of energies required to generate complete displacements, which we've computed for armchair and zigzag chiralities (see Supplemental Material³⁵). The displacement probability calculations reveal a smooth onset in $P_d(E)$ in contrast to what would be expected with the

assumption of a fixed E_d , above which $P_d(E \geq E_d) = 1$. Furthermore, the range of kinetic energies between the onset of non-zero $P_d(E)$ (i.e., $P_d(E = E_d) > 0$) and the maximum $P_d(E \geq E_d) \sim 1$ has both chirality and diameter dependence. Notably, comparison of the chirality and diameter-dependent trends in the onset of non-zero $P_d(E)$ values are congruent with the respective trends obtained in the heuristic $E_d \Phi_C^-$ analysis, substantiating the quality of the heuristic results.

V. CONCLUSIONS

Threshold displacement energies for graphene and SWCNTs have been determined using classical molecular dynamics. These results offer new physical insight into the chirality dependence of E_d and provide a comprehensive classical molecular dynamics benchmark of E_d across 216 chiralities for nine different combinations of irradiation particle, empirical potential, and direction of radial momentum transfer.

Typically, E_d is treated as a singular value for all particles (e.g., electrons, protons, and cosmic rays) since the energy of the particles are much greater than E_d and the energy is transferred to the PKA via a short impulse. These assumptions are largely valid except when the ion energy is near threshold (i.e., the energy of the ion is such that the maximum energy it can transfer to the PKA is $\sim E_d$), in which case its presence affects the subsequent dynamics of the PKA and appear to reduce the E_d for radially inward momentum transfer conditions. Therefore, the E_d is likely to be different for other ions (Ar or Xe), but only when the ion energies are “near threshold”. Although such findings seem intuitive, these results are contrary to the common assumptions in the field, and should be included in future radiation studies.

We acknowledge that the empirical potentials are parameterized to fit equilibrium material properties, making the accuracy of dynamical properties obtained from them through classical MD uncertain. However, the results highlight new chirality dependent trends in E_d , and they predict differences in E_d depending on the irradiation source and direction of radial momentum transfer. Moreover, the $\Phi_e^- E_d$ trends are consistent with experimental diameter-dependent trends of the irradiation stability of SWCNTs under electron irradiation. Since there are limited *ab initio* studies that have explicitly included an ion in determining the E_d in graphene and SWCNTs, these results motivate further computational and experimental studies into this matter.

ACKNOWLEDGMENTS

This research was supported through funding from the U.S. Government through the Defense Threat Reduction Agency (DTRA) under Grant HDTRA-1-10-1-0122. This material is based upon work funded in whole or in

part by the U.S. Government, and any opinions, findings, conclusions, or recommendations expressed in this material are those of the author(s) and do not necessarily

reflect the views of the U.S. Government. A.M. is grateful to Dr. Lucas Lindsay and Prof. Robert Merrill for helpful feedback and discussions.

-
- ¹ M. S. Dresselhaus, G. Dresselhaus, J. C. Charlier, and E. Hernández, *Phil. Trans. R. Soc. A* **362**, 2065 (2004).
 - ² D. S. L. Abergel, V. Apalkov, J. Berashevich, K. Ziegler, and T. Chakraborty, *Advances in Physics* **59**, 261 (2010).
 - ³ A. V. Krasheninnikov and F. Banhart, *Nat. Mater.* **6**, 723 (2007).
 - ⁴ C. D. Cress, C. M. Schauerman, B. J. Landi, S. R. Messenger, R. P. Raffaele, and R. J. Walters, *J. Appl. Phys.* **107**, 014316 (2010).
 - ⁵ C. D. Cress, J. J. McMorro, J. T. Robinson, B. J. Landi, S. M. Hubbard, and S. R. Messenger, *Electronics* **1**, 23 (2012).
 - ⁶ J. E. Rossi, C. D. Cress, A. R. Helenic, C. M. Schauerman, R. A. DiLeo, N. D. Cox, S. R. Messenger, B. D. Weaver, S. M. Hubbard, and B. J. Landi, *J. Appl. Phys.* **112**, 4314 (2012).
 - ⁷ G. H. Kinchin and R. S. Pease, *Rep. Prog. Phys.* **18**, 1 (1955).
 - ⁸ M. J. Norgett, M. T. Robinson, and I. M. Torrens, *Nucl. Eng. Des.* **33**, 50 (1975).
 - ⁹ J. F. Ziegler, M. D. Ziegler, and J. P. Biersack, *Nucl. Instr. Meth. Phys. Res. B* **268**, 1818 (2010).
 - ¹⁰ U. Bangert, W. Pierce, D. M. Kepaptsoglou, Q. Ramasse, R. Zan, M. H. Gass, J. A. Van den Berg, C. B. Boothroyd, J. Amani, and H. Hofss, *Nano Letters* **13**, 4902 (2013).
 - ¹¹ V. H. Crespi, N. G. Chopra, M. L. Cohen, A. Zettl, and S. G. Louie, *Phys. Rev. B* **54**, 5927 (1996).
 - ¹² F. Banhart, J. X. Li, and A. V. Krasheninnikov, *Phys. Rev. B* **71**, 241408 (2005).
 - ¹³ A. V. Krasheninnikov, F. Banhart, J. X. Li, A. S. Foster, and R. M. Nieminen, *Phys. Rev. B* **72**, 125428 (2005).
 - ¹⁴ A. Zobelli, A. Gloter, C. P. Ewels, G. Seifert, and C. Colliex, *Phys. Rev. B* **75**, 245402 (2007).
 - ¹⁵ J. Kotakoski, J. C. Meyer, S. Kurasch, D. Santos-Cottin, U. Kaiser, and A. V. Krasheninnikov, *Phys. Rev. B* **83**, 245420 (2011).
 - ¹⁶ J. Kotakoski, D. Santos-Cottin, and A. V. Krasheninnikov, *ACS Nano* **6**, 671 (2012).
 - ¹⁷ A. V. Krasheninnikov, Y. Miyamoto, and D. Tománek, *Phys. Rev. Lett.* **99**, 016104 (2007).
 - ¹⁸ O. Lehtinen, J. Kotakoski, A. V. Krasheninnikov, A. Tolvanen, K. Nordlund, and J. Keinonen, *Phys. Rev. B* **81**, 153401 (2010).
 - ¹⁹ E. H. Åhlgren, J. Kotakoski, and A. V. Krasheninnikov, *Phys. Rev. B* **83**, 115424 (2011).
 - ²⁰ C. Zhang, F. Mao, F.-S. Zhang, and Y. Zhang, *Chem. Phys. Lett.* **541**, 92 (2012).
 - ²¹ Z. Wang, F. Gao, J. Li, X. Zu, and W. J. Weber, *J. Appl. Phys.* **106**, 4305 (2009).
 - ²² J. Kotakoski, C. H. Jin, O. Lehtinen, K. Suenaga, and A. V. Krasheninnikov, *Physical Review B* **82**, 113404 (2010).
 - ²³ J. Tersoff, *Phys. Rev. B* **39**, 5566 (1989).
 - ²⁴ D. W. Brenner, O. A. Shenderova, J. A. Harrison, S. J. Stuart, B. Ni, and S. B. Sinnott, *J. Phys.: Condens. Matter* **14**, 783 (2002).
 - ²⁵ L. Malerba and J. M. Perlado, *Phys. Rev. B* **65**, 045202 (2002).
 - ²⁶ K. Nordlund, J. Wallenius, and L. Malerba, *Nucl. Instr. Meth. Phys. Res. B* **246**, 322 (2006).
 - ²⁷ M. Robinson, N. A. Marks, K. R. Whittle, and G. R. Lumpkin, *Phys. Rev. B* **85**, 104105 (2012).
 - ²⁸ See Supplemental Material at [URL] for details of the fixed-interval energy ramp method for computing displacement probability curves and its application to a small subset of achiral SWCNTs.
 - ²⁹ S. Plimpton, *J. Comput. Phys.* **117**, 1 (1995).
 - ³⁰ H. J. C. Berendsen, J. P. M. Postma, W. F. van Gunsteren, A. DiNola, and J. R. Haak, *J. Chem. Phys.* **81**, 3684 (1984).
 - ³¹ LAMMPS shrink-wrapped boundary conditions are non-periodic boundaries which automatically adjust the simulation box along the specified axis so as to encompass the atoms no matter how far they move.
 - ³² L. Lindsay and D. A. Broido, *Phys. Rev. B* **81**, 205441 (2010).
 - ³³ J. F. Ziegler, J. P. Biersack, and U. Littmark, *Stopping and Range of Ions in Matter*, Vol. 1 (Pergamon Press, 1985).
 - ³⁴ J. H. Warner, F. Schäffel, G. Zhong, M. H. Rummeli, B. Büchner, J. Robertson, and G. A. D. Briggs, *ACS Nano* **3**, 1557 (2009).
 - ³⁵ See Supplemental Material at [URL] for details of the fixed-interval energy ramp method for computing displacement probability curves and its application to a small subset of achiral SWCNTs.